# OG-HFYOLO :ORIENTATION GRADIENT GUIDANCE AND HETEROGENEOUS FEATURE FUSION FOR DEFORMATION TABLE CELL INSTANCE SEGMENTATION \*

# Long Liu

Nanchang Hangkong University 2304081200008@stu.nchu.edu.cn

# Cihui Yang\*

Nanchang Hangkong University yangcihui@nchu.edu.cn

### **ABSTRACT**

Table structure recognition is a key task in document analysis. However, the geometric deformation in deformed tables causes a weak correlation between content information and structure, resulting in downstream tasks not being able to obtain accurate content information. To obtain fine-grained spatial coordinates of cells, we propose the OG-HFYOLO model, which enhances the edge response by Gradient Orientation-aware Extractor, combines a Heterogeneous Kernel Cross Fusion module and a scale-aware loss function to adapt to multi-scale objective features, and introduces mask-driven non-maximal suppression in the post-processing, which replaces the traditional bounding box suppression mechanism. Furthermore, we also propose a data generator, filling the gap in the dataset for fine-grained deformation table cell spatial coordinate localization, and derive a large-scale dataset named Deformation Wired Table (DWTAL). Experiments show that our proposed model demonstrates excellent segmentation accuracy on all mainstream instance segmentation models. The dataset and the source code are open source: https://github.com/justliulong/0GHFY0LO.

**Keywords** Deformation table cell localization · Instance segmentation · Gradient Orientation-aware Extractor · HHeterogeneous Kernel Cross Fusion

# 1 Introduction

In the digital age of increasing information, tables, as the core carrier of structured data, widely carry key information such as financial reports, education and learning, and scientific experimental data. At the same time, with the popularization of scanning, photography and other technologies, the scene of electronic documents of tables is becoming more and more complex. Especially in the case of complex and changing conditions of illumination, angle and scene conditions, the scanned table images or photographed table images may have various deformations. These physical deformations (such as bending, perspective distortion, and folds) bring great challenges to table structure recognition technology.

The table structure recognition technology [1], which aims at reconstructing the row-column topology and semantic information of a table from an image, has made significant progress through deep learning. Although there are many end-to-end models, which realize the transition from image to structure sequence by directly generating HTML or LaTeX table structure sequences [2, 3], but the black-box feature of end-to-end models makes the intermediate steps uncontrollable. In contrast, the non-end-to-end strategy, a modular approach that decouples cell localization and structural inference, provides a relatively more transparent solution for the table structure recognition task, which also creates the need for cell space coordinates localization. This topic takes the acquisition of cell space coordinates as the research content and studies a method that can effectively extract cell space coordinates in severely deformed tables.

The spatial coordinate localization of table cells can be primarily divided into two methods. One is object detection based on cell contours, which effectively detects most cells with mild deformation, but in the case of serious deformation, this detection method may lose the key information of the cell content, resulting in weak correlation between the cell's

<sup>\*</sup>Corresponding author

content information and the structure, which brings difficulties to downstream tasks (such as cell content acquisition). The other is text box based segmentation[4, 5], mainly applied in wireless non-deformed tables but has not been widely used in wired deformed tables. So there is still a gap in the acquisition of spatial coordinates of wired table cells with severe deformation. Simply using keypoint-based object detection cannot solve the problem of deformed images (as shown in Figure 1b). To address this gap, this study proposes an instance segmentation-based framework (Fig. 1c) that achieves finer-grained spatial coordinate localization, which can effectively provide more accurate and rich information for downstream tasks.



Figure 1: (a) shows a deformed table under natural scene, (b) demonstrates the detection results by contour corner-points, and (c) presents the instance segmentation-based contour, as shown, instance segmentation maintains complete content in deformed cells, providing richer information for downstream tasks like content restoration.

On one hand, there are still some gaps in the datasets for deformed wire table recognition tasks. According to public literature, only a few large-scale open-source datasets like WTW[6] and TAL-OCR[7] target deformed table scenarios, but their annotation granularity is difficult to support the training of pixel-level segmentation models. To address this, we design a data generator that can generate new datasets based on existing datasets. Specifically, we select mildly deformed tables from TAL-OCR and WTW, convert their labels into finer-grained segmentation annotations, and feed this annotated data into the data generator to generate a large amount of deformed table data, effectively supporting instance segmentation model training. Based on some data from the open-source datasets TAL-OCR and WTW, as well as 150 images collected and labeled offline, we derive a large-scale dataset through the data generator and divide it into two independent parts according to the sources: Deformed Wire Table for Small (DWTAL-s) with 8,765 simpler tables mainly derived from TAL-OCR, and Deformed Wire Table for Large (DWTAL-l) containing 19,520 complex tables mainly expanded from WTW. Subsequent experiments focus on these two datasets.

On the other hand, two key challenges emerge when using instance segmentation for the spatial localization of cells in deformed wire tables: Firstly, the highly dense arrangement of table cells and their shared contour lines between adjacent cells make boundary information extraction difficult. Secondly, the existence of merged cells leads to great variation in cell scales, including excessively wide-flat or narrow-tall cells, further complicating the spatial localization of cells.

Instance segmentation is dedicated to achieving pixel-level object separation and semantic parsing, and its method reflects the exploration of the balance between accuracy and efficiency in computer vision. Early studies mainly relied on two-stage frameworks. A representative work, Mask R-CNN [8], achieved highly accurate mask predictions in complex scenes by generating region proposal and extracting features. However, such method is difficult to meet real-time application requirements due to the inherent latency of multi-stage computational processes. With the rise of the single-stage method, researchers have discarded the region proposal mechanism, and instead directly generate object locations and masks through intensive prediction of the global feature map. Nevertheless, single-stage models still face significant challenges in terms of object outlines complexity and dense object differentiation, and need to achieve accuracy breakthroughs through innovations in feature expression mechanisms.

In order to solve the challenges of dense objectives and large-scale changes brought by the derived dataset, we firstly propose a Gradient Orientation-aware Extractor (GOE), which integrates the gradient direction and gradient strength of the image texture into the YOLO-structured network as the learning features and can capture the boundary information of each cell more adequately. Meanwhile, the model combines the bottleneck structure [9] and Heterogeneous Kernel Select Protocol [10] (HKSP) in the feature fusion stage, which can more effectively fuse the features of different scales and improve the detection effect of the model in the case of large-scale changes. Additionally, a scale-aware loss function is designed for segmentation tasks, which adaptively sets higher loss weights to smaller objectives to improve model robustness to scale variations. In the post-processing stage, the traditional instance segmentation model usually follows the non-maximal suppression mechanism based on the bounding box; however, due to the densely arranged deformed cells with complex shapes, the bounding box will have a high degree of overlapping phenomenon, which will lead to the boundary box-based NMS incorrectly suppressing the correct objective. For this reason, we introduce the

mask-based NMS, which directly performs suppression judgment based on the intersection over union of the predicted masks. The main contributions of this work are summarized as follows:

- To address objective omission caused by densely arranged cells in deformed tables, we propose Gradient Orientation-aware Extractor (GOE) that enhances boundary discrimination capability for densely arranged cells. The GOE integrates dual cues of gradient intensity and orientation: During feature extraction, directional filters decouple the image gradient field to quantify intensity distribution in edge regions, preventing isotropic diffusion of conventional convolution kernels along edges. Concurrently, an orientation-aware attention mechanism is designed to encode gradient directions as channel components, guiding the deep layers of the network to focus on discriminative regions of deformation boundaries. we also proposes a Heterogeneous Kernel Cross Fusion (HKCF) module for feature fusion stage. This module dynamically adapts feature representation for multi-scale objectives through the Heterogeneous Kernel Select Protocol (HKSP), deploying asymmetric convolution kernels in parallel. By integrating cross-layer feature interaction mechanisms, the HKCF explicitly captures differentiated spatial patterns of horizontally wide cells and vertically narrow cells.
- we further designs a scale-aware loss function that assigns adaptive weights to objective based on their scales, enhancing the model's sensitivity to smaller deformed cells while suppressing feature redundancy in larger ones. Furthermore, to prevent valid cells from being erroneously suppressed during post-processing due to complex shapes and dense arrangements of deformed cells, we abandon conventional bounding box-based non-maximum suppression (NMS) and introduce a mask-driven NMS post-processing operation.
- To address the scarcity of fine-grained annotated datasets for deformed tables, we designed a data generator that expand existing datasets. We first select mildly deformed tables from available datasets, converting their labels into finer-grained segmentation annotations. These curated samples are then processed by the generator to derive two datasets with varying difficulty levels and scales: DWTAL-s and DWTAL-l.

## 2 Related Work

## 2.1 Spatial coordinate localization of table cells

The spatial coordinate localization of table cells, as an upstream task in table structure recognition, plays a crucial role in subsequent table structure recognition and parsing tasks. To address cell localization, researchers have proposed various approaches. For instance, Prasad et al. [4] introduced CascadeTabNet, which treats text boxes in tables as objectives and formulates text box detection as an instance segmentation task. Built upon Cascade Mask R-CNN, the model extracts text box masks. This represents the first application of instance segmentation algorithms in table structure recognition. However, their experiments were limited to non-deformable tables, and the impact of empty cells on downstream tasks was not thoroughly discussed.

Following a similar concept, Qiao Liang et al. [5] developed the LGPMA model, which integrates global and local information through a soft feature pyramid while also employing instance segmentation for text box detection. Unlike CascadeTabNet, LGPMA incorporates a dedicated search algorithm for empty cells. Regrettably, this model was not evaluated on deformable tables either. To address spatial coordinate extraction in deformable tables, Cycle-CenterNet [6] proposed a contour corner point-based object detection approach that predicts four contour points by detecting cell centers. While advancing deformable table recognition, this method faces limitations: severe boundary curvature significantly increases regression difficulty for corner points, and critical information in certain cells may be lost when using coarse-grained object detection frameworks.

These challenges highlight the need for finer-grained techniques to preserve essential cell information. Motivated by this requirement, our work introduces instance segmentation technology into spatial coordinate localization for deformable tables. By leveraging the pixel-level precision of instance segmentation, our approach achieves more refined spatial coordinate extraction, thereby better addressing the challenges of cell localization in deformable table structures.

#### 2.2 Existing dataset

The development of table structure recognition has been propelled by numerous open-source datasets. Early datasets like UNLV [11] and ICDAR-2013 [12] were primarily designed for evaluating traditional methods, containing limited samples (typically under 1,000 images) and lacking spatial coordinate annotations for table cells. These limitations reduce their utility for modern deep learning-based modular table recognition pipelines. As deep learning demands increasingly larger datasets, researchers like Xu Zhong and Minghao Li introduced large-scale datasets such as PubTabNet [2] and TableBank [13]. However, these datasets focus on structural annotations using HTML or LaTeX sequences while neglecting spatial coordinate labeling. Similarly, large-scale datasets like FinTabNet [14] and SciTSR

[15] include cell coordinates and row-column relationships but primarily data derived from structured digital documents, such as PDFs or documents exported from LaTeX, which exhibit a high degree of standardization, failing to address deformable table recognition.

Although ICDAR-2019 [16] attempted to bridge this gap by introducing scanned archival documents, its small scale (750 images) and limited deformation types remain insufficient. The CamCap [17] dataset, explicitly designed for rule-based algorithms, contains only 85 deformed tables—far too small to support data-driven deep learning models. Until the WTW[6] dataset was proposed which captures tables in diverse natural scenes with complex backgrounds and extensive deformations. However, WTW employs coarse-grained spatial coordinate annotations based on four contour corner points, which struggle with severe deformations. Similarly, the education-focused TAL-OCR [7] dataset, collected from real-world photography, includes moderate deformations but also lacks fine-grained instance segmentation-level spatial annotations for cells. None of these datasets adequately address the challenges of recognizing heavily deformed table structures.

## 2.3 Improvement of instance segmentation in YOLO

Compared to two-stage instance segmentation models, single-stage YOLO-based models demonstrate a balanced performance in both speed and accuracy for instance segmentation tasks, attracting extensive research efforts to enhance the YOLO framework. For example, YOLOMask [18] and PR-YOLO [19] integrated the CBAM module into YOLOv5 [20] to reduce background noise interference. Similarly, YOLO-SF [21] incorporated the CBAM module into YOLOv7 [22] to improve sensitivity to small object features. YOLO-CORE [23] proposed multi-stage constraints (polar coordinate distance loss and sector loss) for direct contour regression to enhance mask boundary precision. YUSEG [24] combined UNet with YOLOv4 [25] to address ambiguous segmentation in dense objects. TTIS-YOLO [26] improved instance segmentation accuracy in complex road scenes through multi-scale efficient cross-stage modules, bidirectional cross-scale connections, and dynamic gradient optimization. GHA-Inst [27] alleviated instance occlusion and background interference by refining YOLOv7's feature fusion and output layers while introducing a Global Hybrid Attention (GHA) module to enhance critical feature retention.

While these advancements cater to diverse scenarios, no existing studies, to the best of our knowledge, have applied YOLO-based segmentation models to spatial coordinate localization of cells in deformable tables. This task presents significant challenges due to extreme variations in object scales, complex cell shapes, and dense arrangements of objectives.

# 3 Data generator and derivative dataset

This section first introduces the implementation of the data generator, and then briefly presents the dataset DWTAL derived from the data generator.

## 3.1 Data generator

Deep learning is inherently data-driven, where the scale and quality of datasets significantly influence model performance. To generate a sufficiently large and high-quality dataset, we propose a data generator designed to create distorted images and corresponding labels from existing images and annotations. The distortions are carefully crafted to simulate real-world deformation scenarios. Specifically, the generator incorporates two distortion methods: wave warping and cylindrical warping. Additionally, it adjusts image brightness based on the original illumination to mimic natural lighting variations in real-world photography. The following three subsections detail the implementation of these two distortion techniques and the strategy for brightness adjustment.

### 3.1.1 Wave distortion transformation

Wave warping is a wave-like warping of images based on trigonometric functions. This technique is designed to mimic distortions caused by attaching images to flexible curved surfaces (e.g., corrugated pipes or folded fabrics), which induce sine or cosine function-based warping, or to imitate human-induced distortions. Such warping introduces severe deformations that significantly challenge table structure recognition. The specific trigonometric warping transformation is defined by Equation 1:

$$\begin{bmatrix} x \\ y \end{bmatrix} + \begin{bmatrix} A \cdot \sin\left(\frac{2\pi y}{\omega}\right) \\ A \cdot \cos\left(\frac{2\pi x}{\omega}\right) \end{bmatrix} = \begin{bmatrix} x' \\ y' \end{bmatrix}$$
 (1)

where x and y denote the coordinates in the original image, while x' and y' represent the coordinates after distortion. The parameter  $\omega$  corresponds to the wavelength, which controls the distortion period (the larger the value of  $\omega$ , the

shorter the distortion period, resulting in more frequent image perturbations). The amplitude A controls the distortion intensity, with higher values of A leading to more severe deformations. Both  $\omega$  and A are adjustable parameters.

#### 3.1.2 Cylindrical distortion transformation

Cylindrical warping deforms image content to simulate cylindrical surface distortions. This method mimics deformations caused by bounding line compression in books or reports, photographs of cylindrical surfaces, or curved distortions from photographing a document held aloft. Such deformations are highly prevalent in real-world scenarios and focus on practical requirements for document upright orientation. Consequently, the warping transformation is applied exclusively along the document's vertical orientation (y-axis), without distorting the horizontal axis (x-axis). The cylindrical warping transformation is defined in Equation 2:

$$\begin{bmatrix} x \\ y \cdot \cos\left(\frac{F \cdot \left(x - \frac{W}{c}\right)}{\frac{W}{c}}\right) \end{bmatrix} = \begin{bmatrix} x' \\ y' \end{bmatrix}$$
 (2)

where x and y denote the original image coordinates, x' and y' represent the warped coordinates, W is the image width, F serves as the distortion factor (with higher values of F resulting in more pronounced distortion), and c defines the warping axis parameter. The param  $\frac{W}{c}$  specifies the central axis of cylindrical curvature. Larger values of c shift the axis leftward, near the axis to undergo milder distortion, while those farther away experience stronger warping. Both F and c are adjustable parameters in the formula.

#### 3.1.3 Illumination adjustment mechanism

Photographic images in real-world scenarios often exhibit shadows due to lighting angles, with shadow locations varying based on illumination direction. Most shadows originate from camera equipment, with the darkest areas typically localized near one of the four image corners. We proposed the illumination adjustment mechanism, which first calculates the overall image brightness using Equation 3, derived from the standard-definition television standard ITU-R BT.601[28]:

$$L = 0.2989 \times R + 0.587 \times G + 0.114 \times B \tag{3}$$

where R, G, B represent the luminance values of the red, green, and blue channels in the image background, respectively, while L denotes the overall brightness (higher L values indicate brighter images).

If the image brightness falls below a predefined threshold, no additional shadows are applied. Otherwise, a shadow center is randomly selected near one of the four image vertices, and per-pixel brightness values are recomputed as follows:

$$I(x,y) = EB + (CB - EB) \cdot \frac{d_{center}(x,y)}{d_{max}}$$
(4)

where CB denotes the Center Brightness (peak shadow intensity, with values in [0,1] where higher values indicate greater brightness), EB represents Edge Brightness (weakest shadow intensity, also within [0,1]),  $d_{max}$  is the image diagonal length, and  $d_{center}(x,y)$  measures the Euclidean distance between pixel (x,y) and the shadow center. Both CB and EB serve as adjustable parameters.

The data generator integrates these three operations (wave distortion, cylindrical warping, and illumination adjustment) through coordinated parameter randomization. Parameter constraints imitate natural deformations: for instance, A and  $\omega$  in Equation 1 maintain an inversely proportional relationship, while F and c in Equation 2 are constrained to avoid extreme values. These inter-parameter dependencies guide the system toward generating physically plausible image distortions.

## 3.2 Derived dataset DWTAL

The data generator enables large-scale deformed tabular data synthesis from limited mildly deformed tables. While the dataset incorporates 150 self-collected samples, it primarily leverages two public natural scene datasets (TAL-OCR and WTW). Initially, mildly deformed tables from TAL-OCR and WTW are selected to generate fine-grained segmentation masks using corner coordinates. These masks are then iteratively processed by the data generator to produce diverse deformed table images. The two source datasets exhibit distinct characteristics: TAL-OCR contains education-oriented images with clear table structures and simplified backgrounds, leading to relatively simpler derived data. To enhance diversity, self-collected samples are merged with TAL-OCR-derived data to form a compact dataset named DWTAL-s. In contrast, WTW features more complex backgrounds and richer content, enabling the creation of a larger, more challenging dataset called DWTAL-1.

**Dataset Splitting.** Both datasets follow identical partitioning protocols. To ensure uniform distribution of deformation types across training and test sets, 80% of each dataset is randomly allocated for training and 20% for testing. Final counts reach 7,012 training and 1,753 test images in DWTAL-s, versus 15,616 training and 3,904 test images in DWTAL-l.

The derived datasets inherit core features from their parent collections, including curved deformations, perspective distortions, multicolor backgrounds, surface irregularities, and illumination variations. A key enhancement lies in the pixel-level instance segmentation annotations for table cells, though all images exclusively contain single-table instances. Additionally, a dataset version with logical coordinate annotations will be publicly released to support broader research applications.

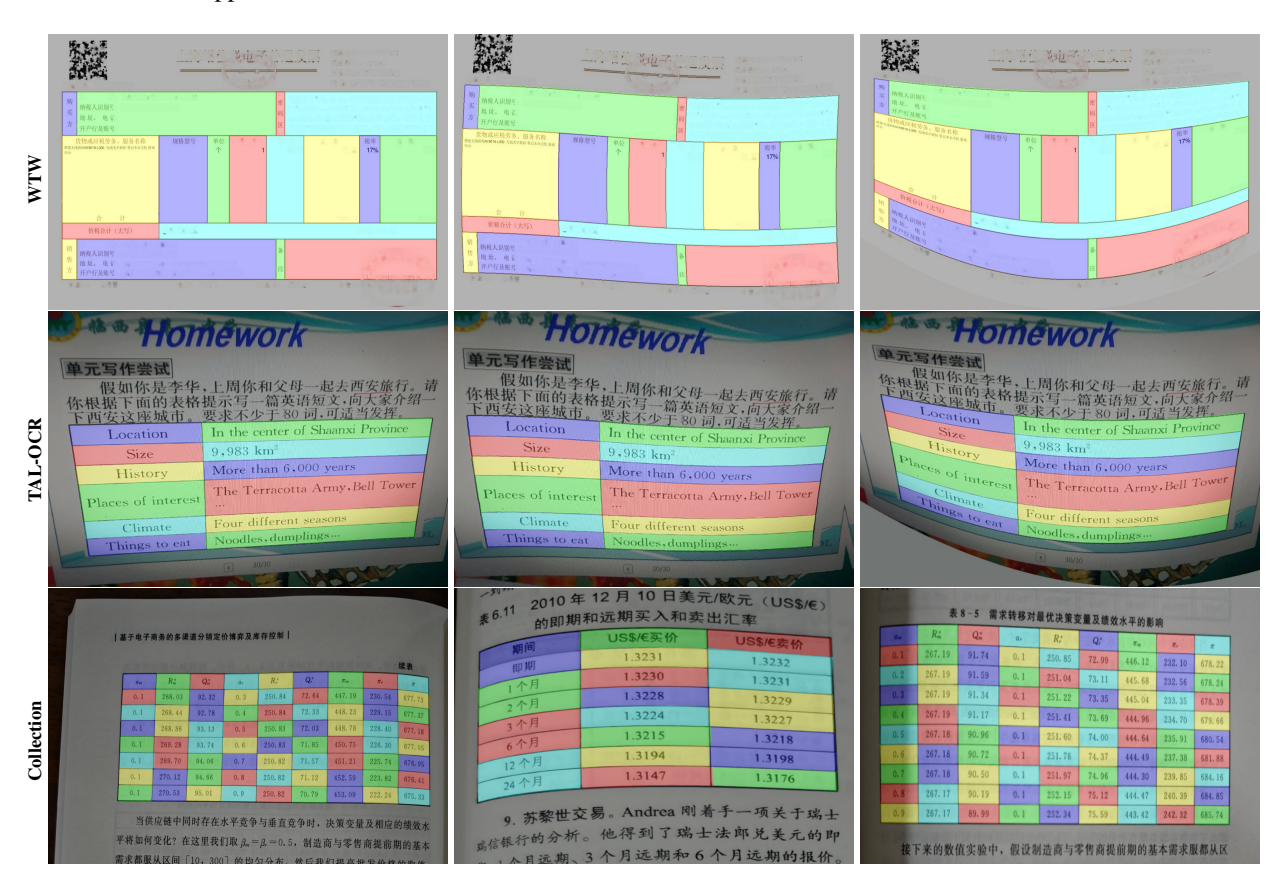


Figure 2: Dataset Annotation Examples: The source of each row's imagery differs: the first row originates from the WTW dataset, the second row is derived from the TAL-OCR dataset, and the third row comprises real-world images collected through offline acquisition.

## 4 Method

#### 4.1 Overall architecture

Figure 3 illustrates the overall architecture of OG-HFYOLO, which adopts a YOLO-like framework divided into three core components: a feature extraction backbone, a feature fusion neck, and a detection head. To enhance texture feature extraction, the model first feeds the initial downsampled feature map into a Gradient Orientation-aware Extractor (GOE), generating feature maps with enriched texture information. The backbone employs CSP-Unit modules, each comprising a  $3 \times 3$  downsampling convolution, SiLU activation, batch normalization, and a Cross-Stage Partial Network (CSP) [29] used by YOLOv5. Through five downsampling operations, the backbone produces multi-scale feature maps P3, P4, P5.

During feature fusion, the extracted features undergo integration via the FPN-PAN [30] pathway. Distinct from standard YOLO implementations, our model incorporates Heterogeneous Kernel Cross Fusion (HKCF) module after skip connections to enhance cross-scale objective feature interactions. The fused features are then processed through

CSP blocks for final refinement before being delivered to the detection head. The detection head retains YOLOv5's anchor-based [31] design, performing classification and bounding box regression using predefined anchor boxes, with Non-Maximum Suppression [32] (NMS) filtering redundant detections.

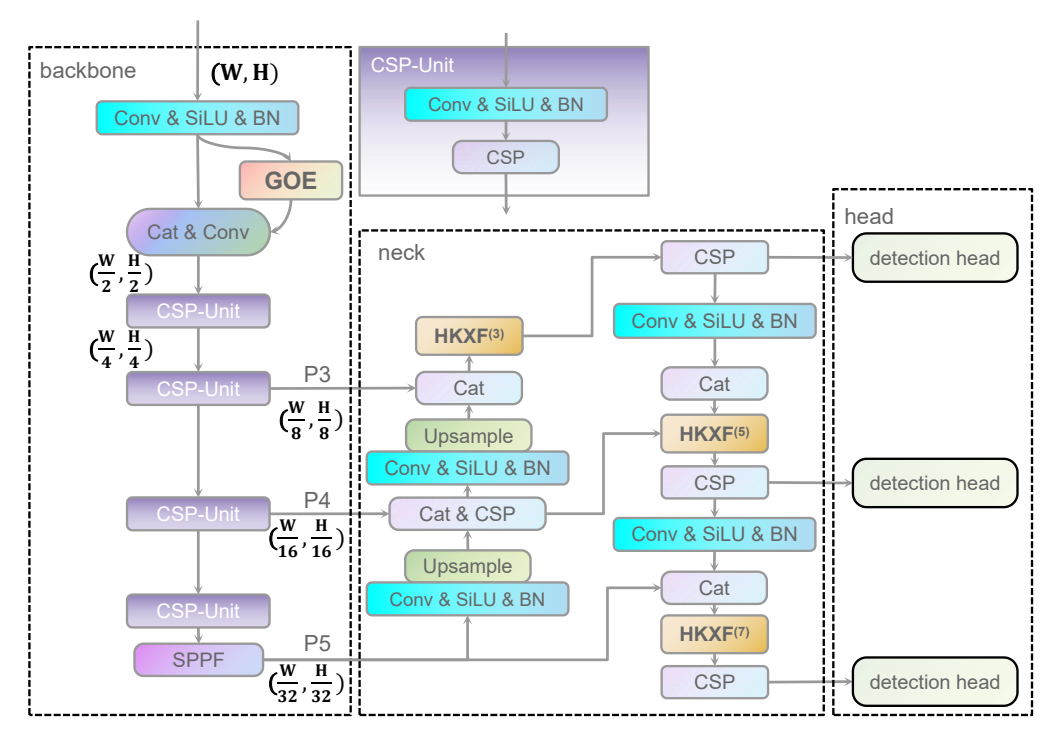


Figure 3: The overview of the OG-HFYOLO.

### 4.2 Gradient Orientation-aware Extractor

We consider object density the primary challenge in spatial coordinate localization for deformed table cells. Inaccurate contour extraction by the model risks merging adjacent small cells into erroneously detected large ones. This aggregation progressively obscures scale variations during feature fusion, ultimately degrading prediction accuracy.

The accuracy of instance segmentation in target-intensive scenarios is limited by the model's ability to perceive contour details, and the essential challenge lies in how to effectively model the gradient strength and orientation sensitivity of texture regions. The Histogram of Oriented Gradients (HOG) [33] offers critical insights here: As shown in Figure 4, HOG divides the image into multiple grids, decouples gradient features into gradient direction and gradient intensity within each grid, and aggregates these attributes into orientation-specific histograms. Its core philosophy lies in simultaneously capturing gradient magnitude and directional priors to enhance the geometric discriminability of contours, a principle that directly informs our approach to addressing contour ambiguity in dense cell detection.

The GOE adopts the same philosophy, focusing on enabling the model to learn both gradient intensity and gradient direction features of contour details, which effectively enhances its recognition capability for targets with complex contours and dense arrangements.

Figure 5 illustrates the internal architecture of the proposed Gradient Orientation-aware Extractor (GOE). The module takes a feature map encoding texture information as input. The GOE first employs distinct decoupling operators (Equation 5) to decompose the input feature map I into a horizontal gradient orientation feature map  $G_x$  and a vertical gradient orientation feature map  $G_y$ . To preserve the directional priors of the decoupling operators  $G_x$  and  $G_y$ , their weights are initialized as conventional edge operators. During training, kernel parameter constraints are relaxed, allowing the network to adaptively adjust gradient response weights based on task requirements (e.g., deformation edge enhancement, noise suppression), thereby overcoming the geometric limitations inherent to standard edge operators.

$$G_x, G_y = \mathcal{G}_x(\mathbf{I}), \mathcal{G}_y(\mathbf{I})$$
 (5)

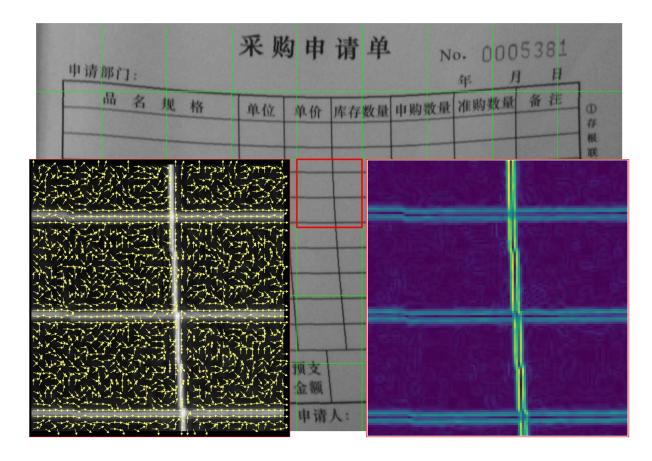


Figure 4: HOG feature extraction core schematic diagram: the left inset demonstrates gradient orientation features within the red grid, while the right inset illustrates gradient magnitude features within the same grid. These two key features allow for comprehensive features of edge texture information.

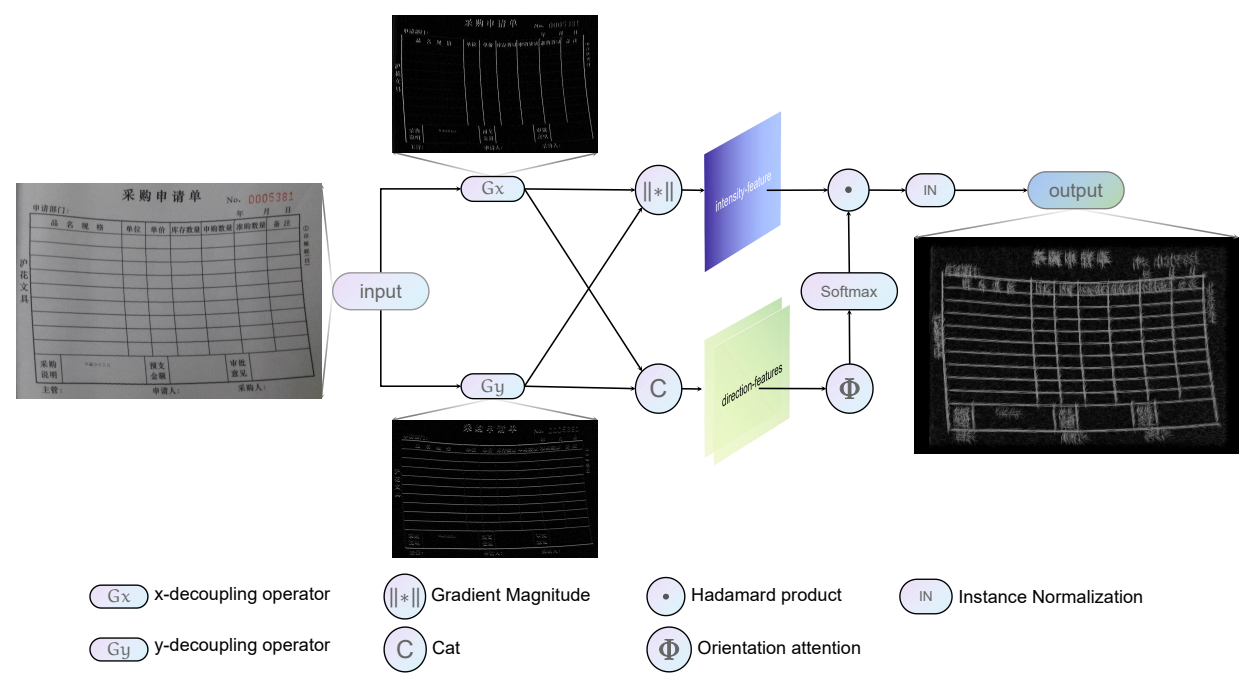


Figure 5: The overall structure of GOE: Feature extraction and combination of gradient direction and gradient magnitude through decoupling and recombination.

After obtaining the decoupled horizontal gradient orientation feature map  $G_x$  and vertical gradient orientation feature map  $G_y$ , the module employs distinct strategies to integrate gradient features from both orientations: on one hand, the GOE calculates gradient magnitude by Equation 6 to generate the gradient intensity feature map  $I_{GM}$ ; on the other hand, the GOE performs channel-wise concatenation according to Equation 7 to derive the gradient orientation feature map  $I_{GD}$ .

$$I_{GM} = \sqrt{G_x^2 + G_y^2} \tag{6}$$

$$I_{GD} = Cat(G_x, G_y) \tag{7}$$

The GOE module ultimately aggregates the gradient intensity feature map  $I_{GM}$  and gradient direction feature map  $I_{GD}$  according to Equation 8. It first applies orientation attention  $\Phi$  to channel-encoded  $I_{GD}$ , mapping gradient information

from distinct orientations into separate channels. The encoded features are then normalized via Softmax[34]. Subsequently, the gradient intensity feature map  $I_{GM}$  is weighted through the Hadamard product with the channel-encoded gradient direction feature map  $I_{GD}$ . Since gradients in each orientation are mutually independent, instance normalization (IN)[35] is adopted to stabilize model training, ultimately yielding the feature output  $I_o$  that simultaneously encapsulates gradient orientation and intensity feature.

$$I_o = IN(Softmax(\Phi(I_{GD})) \odot I_{GM})$$
(8)

Orientation Attention  $\Phi$ : The orientation attention  $\Phi$  in the GOE module is fundamentally a learnable convolutional operation. The module initializes the convolutional kernel weights W by emulating the orientation binning technique used in Histogram of Oriented Gradients (HOG). Specifically, the continuous angular space  $[0,\pi)$  is uniformly discretized into n orientation bins, with the central angle of each bin defined as  $\theta_i = \frac{i\pi}{n}, (i=0,1,...,n-1)$ , For each orientation bin  $\theta_i$ , the corresponding unit directional basis vectors in Cartesian coordinates are computed via the polar coordinate transformation formula:  $[e^i_x = cos(\theta_i), e^i_y = sin(\theta_i)]$ . These basis vectors are then concatenated and expanded across two dimensions to construct the initialized kernel weights  $W \in R^{n \times 2 \times 1 \times 1}$ .

The hierarchical feature learning mechanism of convolutional neural networks demonstrates that shallow high-resolution feature maps exhibit stronger capabilities in capturing low-level visual features such as edges and textures, while deeper layers focus more on semantic abstraction and global structure modeling[36]. Based on this, we embed the Gradient Orientation Extractor (GOE) after the first convolutional downsampling layer in the backbone network, leveraging its high spatial resolution characteristics to precisely capture directional gradient features. Figure 6 illustrates the effectiveness of the GOE module in early-stage feature extraction from the second downsampled feature map. By incorporating the proposed extractor, the network injects geometric priors at early stages for images with chromatic interference and blurred cell contours, which establishes a fine-grained foundation for subsequent cross-layer feature fusion.

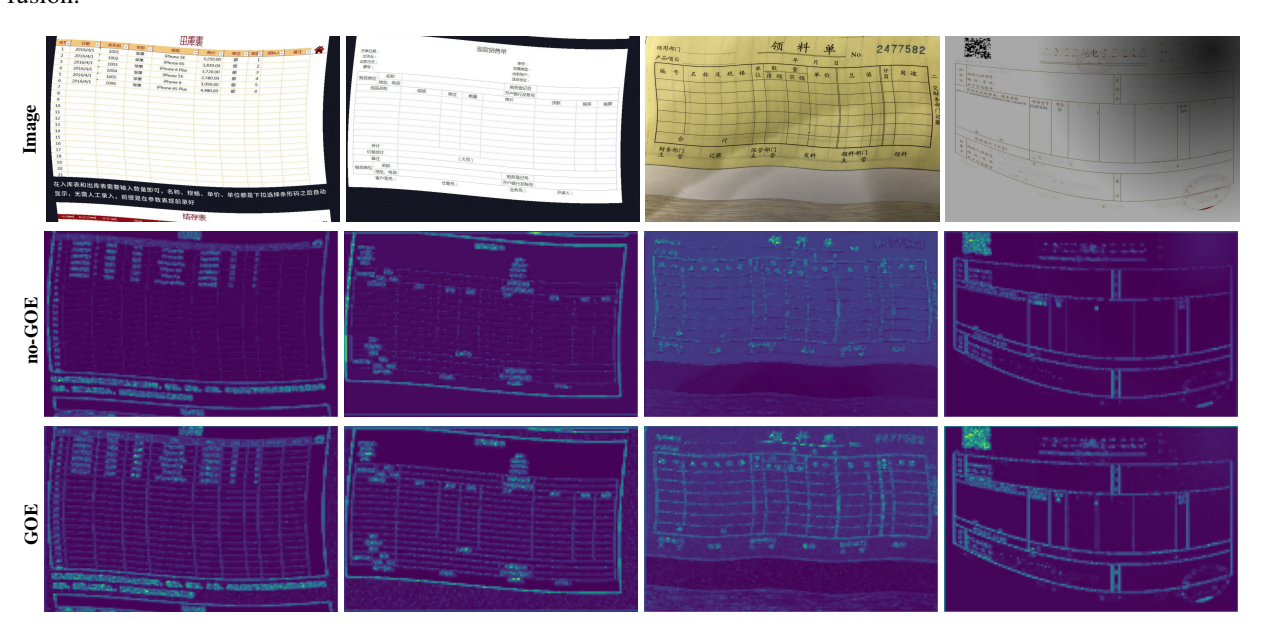


Figure 6: GOE module effect demonstration.

## 4.3 Heterogeneous Kernel Cross Fusion

In addition to dense objective distribution, table cell segmentation also faces challenges arising from extreme scale diversity caused by merged cells: horizontal merging creates wide-spanning targets across multiple columns, while vertical merging generates tall and narrow targets spanning multiple rows. Such objectives require the model to possess multi-granularity perception capabilities. The YOLO series addresses scale variation through multi-scale detection heads, where high-resolution feature maps detect large objectives and low-resolution ones focus on small objectives. However, traditional fixed-size convolutional kernels struggle to adapt to the morphological diversity of cell features in tables. Inspired by YOLO-MS[10], which proposes matching objective diversity through kernel diversity and introduces the Heterogeneous Kernel Selection Protocol[10] (HKSP), we adopt the HKSP concept and integrate asymmetric cross-convolution[37] to design a Heterogeneous Kernel Cross-Fusion (HKCF) module. As shown in

Figure 7, the module employs a bottleneck structure to reduce computational complexity. The input feature map  $I_{in}$  is first channel-reduced via  $1 \times 1$  convolution to obtain low-dimensional features  $F_{in}$ . The HKCF module  $HKCF^{(k)}$  with kernel size k then extracts features  $F_{out}$  in this reduced channel space. Finally,  $F_{out}$  and  $F_{in}$  are concatenated along the channel dimension, and the original channel dimension is restored through another  $1 \times 1$  convolution to output the feature map  $I_{out}$ . The computational flow can be formulated as:

$$F_{in} = Conv(I_{in})$$

$$F_{out} = HKCF^{(k)}(F_{in})$$

$$I_{out} = Conv(Cat(F_{in}, F_{out}))$$
(9)

As shown in Equation 10, within the Heterogeneous Kernel Cross-Fusion module  $HKCF^{(k)}$ , the input feature map  $F_{in}$  first undergoes processing through the Channel Attention Bridge[38] (CAB). The CAB employs global average pooling and a multilayer perceptron to generate channel-wise weights, dynamically enhancing feature channels strongly correlated with target morphology, thereby alleviating information loss caused by the bottleneck structure's dimensionality reduction. To address the extreme narrow-tall and wide-flat challenges posed by merged cells, the module replaces standard convolution with heterogeneous cross convolution  $HKCF^{(k)}$ . This operation deploys horizontally extended kernels  $(1 \times k)$  and vertically extended kernels  $(k \times 1)$  in parallel. These dual branches respectively capture horizontal continuity features for column-spanning merged cells and vertical long-range dependencies for row-spanning merged cells. The outputs of these two branches sum to precisely adapt to the geometric characteristics of targets at varying scales. Following HKSP, cross-convolutions with kernel sizes 3, 5, 7 are progressively applied from shallow to deep feature fusion maps. Finally, the original input  $F_{in}$  is added to the output feature map from  $HXConv^{(k)}$  by residual connection, producing the final output feature map  $F_{out}$ .

$$F_{out} = HXConv^{(k)}(CAB(F_{in})) + F_{in}$$

$$HXConv^{(k)}(I) = HConv^{(k)}(I) + VConv^{(k)}(I)$$
(10)

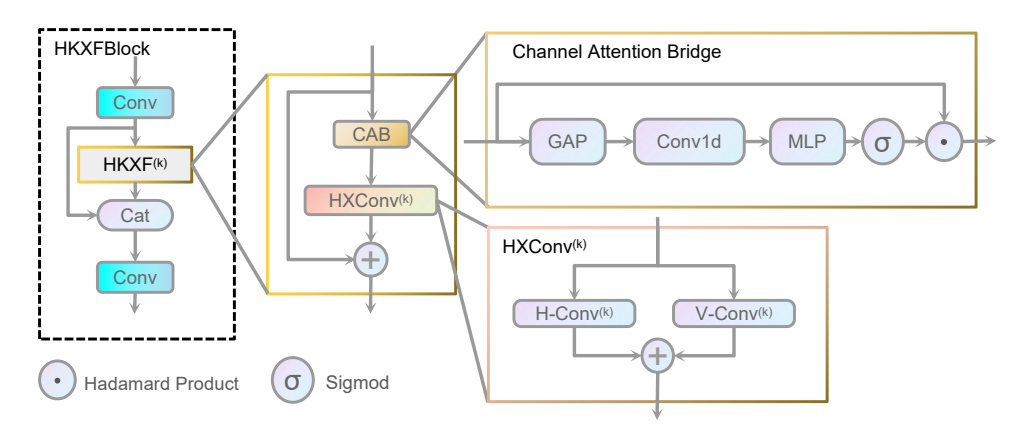


Figure 7: The internal structure of HKCF primarily consists of bottleneck structures and cross-convolutions. CBA is used for dimensionality reduction loss in dense bottleneck structures, and the selection of cross-convolution kernels follows HKSP.

### 4.4 Loss function optimization

In anchor-based instance segmentation frameworks, the object loss  $\mathcal{L}_{obj}$  typically relies on Intersection over Union (IoU) and its variants to measure geometric deviations between predicted and ground-truth bounding boxes. However, the conventional CIoU loss[39] suffers from ambiguous optimization directions for extreme aspect ratio targets due to its coupled computation of aspect ratio and center distance, leading to reduced bounding box regression accuracy. To address this, we replace CIoU with the EIoU loss[40], which explicitly decouples width-height optimization paths, enabling targeted gradient direction adjustment for aspect ratio-sensitive targets.

For mask loss  $\mathcal{L}_{mask}$ , the YOLO framework defaults to binary cross-entropy loss  $\mathcal{L}_{BCE}$  (Equation 11). Additionally, to mitigate the influence of large target areas on loss values, YOLO applies a simple normalization (Equation 12) to the detected target regions within  $\mathcal{L}_{BCE}$ .

$$\mathcal{L}_{BCE} = -\frac{1}{N} \sum_{i=1}^{N} \left[ \mathbf{M}_{gt}^{(i)} \log \mathbf{M}_{pred}^{(i)} + (1 - \mathbf{M}_{gt}^{(i)}) \log(1 - \mathbf{M}_{pred}^{(i)}) \right]$$
(11)

where N denotes the total number of pixels in the mask,  $\mathbf{M}_{\text{gt}}$  represents the ground truth mask, and  $\mathbf{M}_{\text{pred}}$  is the predicted mask.

$$\mathcal{L}_{norm} = \frac{1}{A} \sum_{(x,y) \in crop(\Omega)} \left[ \frac{1}{H'W'} \mathcal{L}_{BEC}(x,y) \right]$$
 (12)

where A indicates the area (pixel count) of the target instance for normalization, while H' and W' represent the height and width of the cropped region  $crop(\Omega)$ , respectively, which can be spatially averaged for loss computation, analogous to global average pooling.

However, relying solely on the binary cross-entropy loss  $\mathcal{L}_{BCE}$  neglects the inherent similarity between cell backgrounds and the overall table background, where background pixels dominate in quantity. To prevent the model from biasing towards the high-frequency background class, we integrate Dice Loss[41] into the base segmentation loss  $\mathcal{L}_{base}$ . Unlike cross-entropy loss, which focuses on per-pixel probability calibration, Dice Loss optimizes for region overlap, prioritizing the structural integrity of segmented targets. This approach enhances edge alignment and regional continuity. The Dice Loss formula is defined in Equation 13, where  $\odot$  denotes element-wise multiplication.

$$\mathcal{L}_{Dice} = 1 - \frac{2 \sum \mathbf{M}_{pred} \odot \mathbf{M}_{gt}}{\sum \mathbf{M}_{pred} + \sum \mathbf{M}_{gt}}$$
(13)

The base loss  $\mathcal{L}_{base}$  is formed by summing the two losses according to Equation 14. In the original loss function, the inverse proportional function for normalization aims to eliminate the influence of target size on loss weighting. While this effectively prevents training bias toward large-target optimization, it adversely affects the optimization of small targets. Specifically, the inverse proportional function applies overly aggressive weighting to losses from small-area targets. To address this issue, this paper reconsiders the allocation of dynamic weights: to avoid excessive weighting amplification for small targets, the proposed dynamic weighting scheme incorporates a smoother logarithmic function on top of the original normalization weights. The calculation is as follows: 15

$$\mathcal{L}_{base} = \mathcal{L}_{BCE} + \mathcal{L}_{Dice} \tag{14}$$

$$W = 1 + \log\left(\frac{1}{A}\right) \tag{15}$$

Integrating the above considerations, we obtain the scale-aware loss function  $\mathcal{L}_{scale-aware}$ , as defined in Equation 16, where n denotes the number of instances in the image,  $H'_i$  and  $W'_i$  represent the height and width of the cropped region for the instance i, and  $A_i$  corresponds to the area of the instance i.

$$\mathcal{L}_{scale-aware} = \frac{1}{n} \sum_{i=1}^{n} \left[ W_{i} \frac{1}{A_{i}} \sum_{(x,y) \in crop(\Omega)} \left[ \frac{1}{H'_{i}W'_{i}} \mathcal{L}_{base}(x,y) \right] \right] \\
= \frac{1}{n} \sum_{i=1}^{n} \left[ \left( 1 + \log \left( \frac{1}{A_{i}} \right) \right) \cdot \frac{1}{A_{i}} \sum_{(x,y) \in crop(\Omega)} \left[ \frac{1}{H'_{i}W'_{i}} \left( \mathcal{L}_{BCE} + \mathcal{L}_{Dice} \right) \right] \right]$$
(16)

# 4.5 Post-process optimization

Anchor-based detection models typically rely on Non-Maximum Suppression (NMS) as a core post-processing operation to filter redundant detection boxes using an Intersection over Union (IoU) threshold. Traditional NMS performs robustly in sparsely distributed object scenarios but exhibits inherent limitations in dense deformed table cell detection: when adjacent cells exhibit highly overlapping bounding boxes due to geometric deformation, the IoU criterion mistakenly identifies them as the same instance, thereby suppressing correctly localized boxes with lower confidence scores. Although Soft-NMS [42] partially alleviates over-suppression through a confidence decay mechanism, severe overlaps caused by complex target shapes still lead to inflated IoU values, failing to address the root cause. To resolve this, inspired by the mask competition strategy in SOLOv2 [43], we abandon the bounding-box suppression paradigm and

introduce Mask-Driven Non-Maximum Suppression, which employs pixel-level Mask\_IoU for redundancy elimination. The metric is defined as:

$$Mask\_IoU = \frac{|M_i \cap M_i|}{|M_i \cup M_j|}$$
(17)

where  $M_i$  and  $M_i$  are binary matrices of two predicted masks. A low-confidence mask is suppressed only if its Mask\_IoU with a higher-confidence mask exceeds the threshold. Compared to the traditional IoU criterion, Mask\_IoU directly quantifies mask overlap, circumventing spatial mismatches induced by bounding box overlaps, thereby preserving more precise cell instances in complex table layouts.

# 5 Experiments

#### 5.1 Experimental settings

The datasets involved in the experiments are DWTAL-s and DWTAL-l, both of which are experimented on an RTX 3090 with 24 GB of video memory, and the whole experiment relies on Python 3.8.19, PyTorch 1.13.0, and CUDA version 12.4.

For ablation studies, we don't use pretrained weights. Input images were resized to  $640 \times 640$ , with a batch size of 2. Training spanned 200 epochs using a Stochastic Gradient Descent (SGD) optimizer configured with momentum factor of 0.9, initial learning rate of 0.001, and weight decay of 0.0005.

In order to facilitate comparison experiments, all non-YOLO-based models were implemented using the MMDetection3 framework [44] on the 24GB RTX 3090 GPU. ResNet-101 backbones were initialized with pretrained weights from Microsoft Research Asia (MSRA) [45], trained on the ImageNet dataset [46]. For DWTAL-s, input images were set to  $640 \times 640$  with a batch size of 2. Due to limited training resources, DWTAL-l experiments also used  $640 \times 640$  inputs but with a reduced batch size of 1. Both datasets underwent 100 epochs of fine-tuning with the SGD optimizer, configured with momentum of 0.9, initial learning rate of 0.001, and weight decay of 0.0001.

#### 5.2 Evaluation metrics

To comprehensively evaluate the performance of instance segmentation models, we adopt general metrics including mean Average Precision (mAP), model parameter count, and GFLOPs as quantitative criteria. mAP measures the model's segmentation and classification capabilities by calculating average precision across multiple confidence thresholds. Specifically, precision P@t and recall R@t at a given confidence threshold t are first computed using Equation 18:

$$P@t = \frac{TP@t}{TP@t + FP@t}, \quad R@t = \frac{TP@t}{TP@t + FN@t}$$
(18)

where FP@t denotes false positives at confidence threshold t, and FN@t represents false negatives at the same threshold.

Average Precision (AP) is defined as the area under the precision-recall (PR) curve. The per-class average precision AP@t at confidence threshold t is calculated via Equation 19:

$$AP@t = \frac{1}{101} \sum_{r \in \{0, 0.01, 0.02, \dots, 1\}} P@t_{interp}(r)$$
(19)

where P@t<sub>interp</sub>(r) denotes the maximum precision when the recall  $R@t \ge r$ .

Finally, the mean Average Precision mAP@t is obtained by averaging the AP@t values across all classes at confidence threshold t using Equation 20. Different confidence thresholds lead to distinct metrics: mAP@50 uses a confidence threshold of 0.5, reflecting baseline performance under lenient localization requirements, while mAP@50:95 rigorously evaluates the model's robustness to object boundaries by averaging results across confidence thresholds from 0.5 to 0.95 with a step size of 0.05.

$$mAP@t = \frac{1}{N_{\text{classes}}} \sum_{i=1}^{N_{\text{classes}}} AP_i@t$$
 (20)

The number of parameters (Parameters) reflects the model's complexity and storage requirements. Excessive parameters may lead to overfitting and deployment challenges, while insufficient parameters can limit feature representation capacity. GFLOPs quantifies the computational demand per inference in billions of floating-point operations, measuring computational efficiency. Models with high GFLOPs rely on high-performance GPUs and struggle to meet real-time requirements, whereas low-GFLOPs designs are suitable for real-time video processing but require architectural optimization to balance accuracy trade-offs. All GFLOPs values in this study are reported under the input size of  $640 \times 640$ .

### 5.3 Quantitative result

To validate the model's effectiveness, we compares the proposed model with mainstream segmentation models on the DWTAL-s dataset, including two-stage models (Mask R-CNN [8], Cascade Mask R-CNN [47]), single-stage models (SOLOv2 [43], YOLACT [48]), Transformer-based architectures (Mask2Former [49]), and classical YOLO models (YOLOv51-seg [20], YOLOv81-seg [50], YOLOv11-seg [51]).

The experimental results on the DWTAL-s dataset, as shown in Table 1, demonstrate that the OG-HFYOLO model achieves a mAP@50:95 of 74.23%, outperforming mainstream two-stage instance segmentation models such as Mask R-CNN (62.5%) and Cascade Mask R-CNN (62.1%). It surpasses classical YOLOv8 (57.5%) and the more advanced YOLOv11 (57.8%) by 16.73% and 16.43%, respectively, and exceeds the highest-precision YOLOv5 variant (71.96%) by 2.27%. Additionally, the proposed model outperforms the Transformer-based Mask2Former (63.3%) by 10.93%. Regarding model parameter count, the introduction of a heterogeneous kernel cross-fusion architecture with relatively large convolutional kernels slightly increases the parameter size, though this remains manageable under current hardware storage constraints. In terms of inference speed, YOLACT has seriously lost model accuracy in the pursuit of extreme speed and model size, while the OG-HFYOLO model balances accuracy and speed, retaining the speed that a single-stage model should have. It surpasses both mainstream two-stage models and some single-stage models like SOLOv2 and Mask2Former in speed.

Table 1: The different model performance on DWTAL-s

Model	Backbone	Para (M)	GFLOPs	Bbox		Mask	
		()		mAP@50	mAP@50:95	mAP@50	mAP@50:95
Mask RCNN[8]	ResNet-101	62.963	245	0.752	0.671	0.736	0.625
Cascade Mask RCNN[47]	ResNet-101	96.013	978	0.752	0.679	0.741	0.621
Mask2Former[49]	ResNet-101	62.995	230	0.742	0.656	0.742	0.644
SOLOv2[43]	ResNet-101	65.221	243	-	-	0.637	0.451
YOLACT[48]	ResNet-101	53.719	84.719	0.692	0.586	0.678	0.482
YOLOv51-seg[20]	<b>CSPDark</b>	92.27	147.5	0.9754	0.9144	0.9665	0.7196
YOLOv8l-seg[50]	<b>CSPDark</b>	88	220.1	0.721	0.684	0.721	0.575
YOLOv111-seg[51]	CSPDark	53.22	141.9	0.721	0.688	0.721	0.578
ours	$CSPDark^*$	125.39	170	0.9896	0.9156	0.9851	0.7423

<sup>\*:</sup>CSPDark\* is based on the normal CSPDark backbone and introduces the GOE module. The overall backbone structure is the same as that of CSPDark.

As shown in Table 2, the proposed model also achieves state-of-the-art segmentation accuracy metrics on the DWTAL-l dataset compared to other mainstream models, demonstrating its generalization capability across diverse datasets.

#### 5.4 Qualitative analysis

Figure 8 presents a comparative visualization of segmentation results across different models. Observations reveal that even seemingly straightforward cases like (a) exhibit severe missed detections in most mainstream models, whereas the proposed model achieves performance comparable to the advanced Mask2Former on this example and outperforms it across all subsequent test images. Among anchor-based models, YOLOv5 demonstrates the second-lowest missed detection rate after our proposed method. However, in scenarios like (d), the bounding box-based non-maximum suppression (NMS) not only suppresses valid cells but also introduces erroneous overlapping detections, as seen in (b) and (e). For images with blurred contours (f) and multi-colored background cells (e), the proposed model leverages its GOE module to achieve optimal detection results. In scale-variant cell detection tasks, such as the elongated cell in the bottom row of (b), SOLOv2 fails to accurately capture cell dimensions, while our model maintains robust performance.

To further demonstrate the generalization capability of the proposed model for table cell segmentation, Figure 9 showcases segmentation results on real-world photography scenarios and images from the Camcap dataset [17], using



Figure 8: Comparison of the effects of different models: Subfigures (a)–(c) are derived from the simpler DWTAL-s dataset, and (d)–(f) originate from the more complex DWTAL-l dataset.

Table 2.	The different	modal	performance of	on DW/TAI 1	
Table 2:	i ne aillerent	modei	performance of	on Dwiat-i	

Model	Backbone	F	Bbox	Mask		
Woder	Buckeone	mAP@50	mAP@50:95	mAP@50	mAP@50:95	
Mask RCNN[8]	ResNet-101	0.524	0.479	0.509	0.447	
Cascade Mask RCNN[47]	ResNet-101	0.524	0.488	0.521	0.451	
SOLOv2[43]	ResNet-101	-	-	0.48	0.39	
YOLACT[48]	ResNet-101	0.446	0.308	0.401	0.225	
YOLOv51-seg[20]	<b>CSPDark</b>	0.860	0.803	0.8338	0.6134	
YOLOv81-seg[50]	<b>CSPDark</b>	0.663	0.627	0.654	0.514	
YOLOv111-seg[51]	CSPDark	0.664	0.633	0.654	0.521	
ours	$CSPDark^*$	0.8685	0.8017	0.8457	0.6238	

a model trained exclusively on DWTAL-l data. The left column displays natural scene photographs: the top-left image originates from real tables in the WTW dataset, and the bottom-left represents actual captured scenes. The right four subfigures correspond to Camcap samples. From the results, the OG-HFYOLO model can still achieve good segmentation results, which is enough to prove that the model has strong generalization ability.

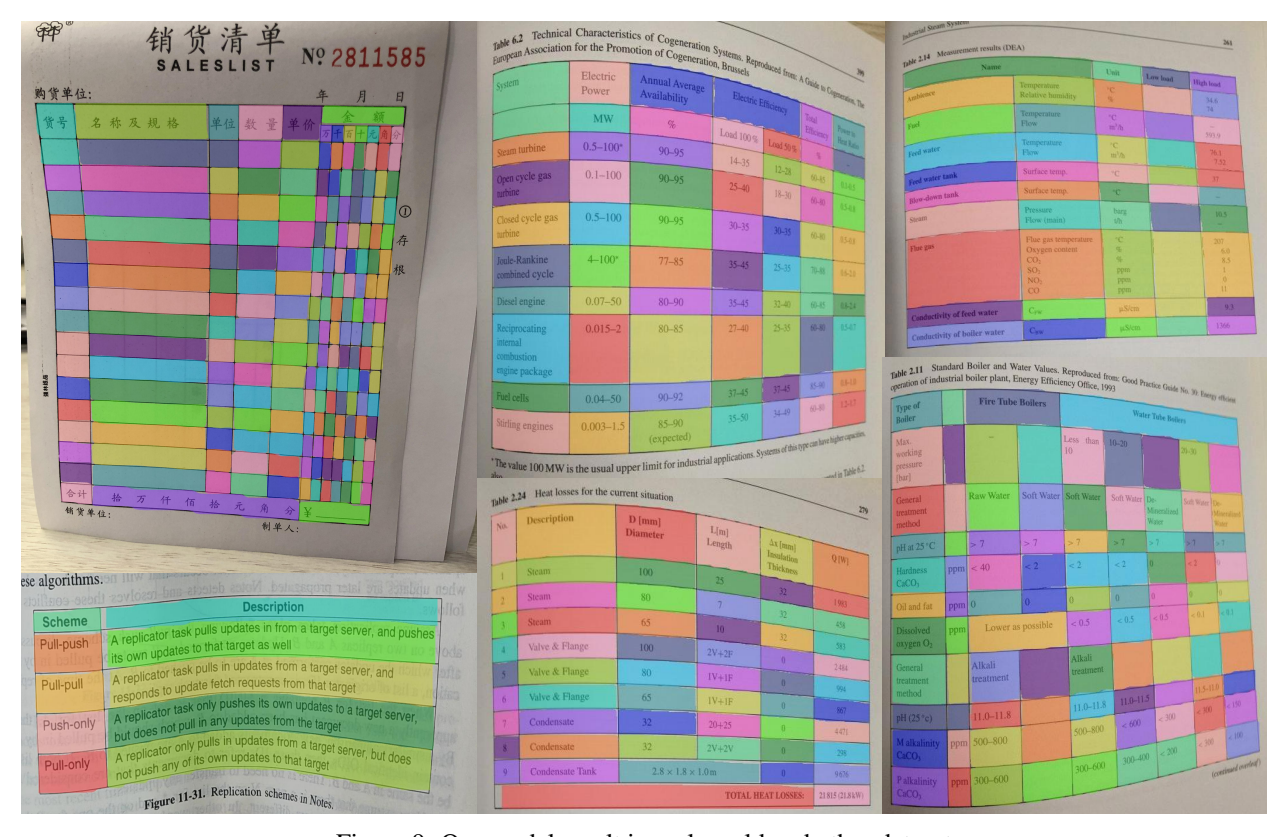


Figure 9: Our model result in real-world and other dataset

## 5.5 Ablation study

# 5.5.1 Impact of Anchor Mechanism

With the advancement of deep learning, detection-oriented models have progressively transitioned from anchor-based to anchor-free [52] mechanisms to pursue higher speed and smaller parameter footprints. Starting from YOLOv5, models began reducing reliance on predefined anchors, and by YOLOv8, anchor-free mechanisms became the standard. Com-

parative experiments clearly demonstrate that YOLOv8l-seg and YOLOv11l-seg, which adopt anchor-free mechanisms, exhibit significantly lower accuracy than their YOLOv5l-seg counterparts within the same YOLO series. To validate the superiority of anchor-based mechanisms for the current task, ablation studies on anchor mechanisms were conducted. As shown in Table 3, across both derived datasets, all metrics for both YOLOv5 and OG-HFYOLO models achieve over 10% significant improvement when using anchor-based mechanisms, highlighting anchor-based effectiveness in this research context.

Table 3: Impact of Anchor Mechanism

Dataset	mode	E	Bbox	Mask			
Dataset	1110 46	mAP@50	mAP@50:95	mAP@50	mAP@50:95		
YOLOv5							
DWTAL-s	anchor-free anchor-base	0.72 <b>0.9754</b>	0.682 <b>0.9144</b>	0.72 <b>0.9665</b>	0.573 <b>0.7196</b>		
DWTAL-I	anchor-free anchor-base	0.664 <b>0.860</b>	0.629 <b>0.803</b>	0.654 <b>0.8338</b>	0.515 <b>0.6134</b>		
OG-HFYOLO							
DWTAL-s	anchor-free anchor-base	0.721 <b>0.9896</b>	0.68 <b>0.9156</b>	0.621 <b>0.9851</b>	0.318 <b>0.7423</b>		
DWTAL-l	anchor-free anchor-base	0.662 <b>0.8685</b>	0.619 <b>0.8017</b>	0.563 <b>0.8457</b>	0.3 <b>0.6238</b>		

### 5.5.2 Effect of the proposed method

Table 4 presents the ablation study results of the proposed method on the DWTAL-s dataset. The Gradient Orientation-aware Extractor (GOE) is designed to capture richer texture information and mitigate detection challenges caused by dense object distributions. The Heterogeneous Kernel Cross Fusion (HKCF) and scale-aware Loss address severe scale and aspect ratio variations, while the MASK-NMS algorithm optimizes post-processing to handle complex shapes and crowded instances. The challenges inherent in the derived dataset are interdependent, meaning solving isolated issues yields limited performance gains. For instance, while texture extraction by GOE partially addresses detection difficulties, it fails to resolve scale variation problems, resulting in marginal improvements (e.g., only a 0.44% increase in mask mAP@50:95 when GOE is introduced alone). Similarly, isolated integration of HKCF and scale-aware Loss improves mask mAP@50:95 by merely 0.09% and 0.48%, respectively. However, as demonstrated in Table 4, synergistic integration of complementary modules yields significant enhancements. For example, combining GOE with scale-aware Loss boosts mask mAP@50:95 by 1.29%. These results confirm that while each proposed module is individually effective, their collaborative integration is essential to achieve optimal performance.

Table 4: Effect of the proposed method

GOE HKCF DWLoss		DWLoss	MASK-NMS	Bbox		Mask		Para (M)	GFLOPs
002	111101	2 11 2000	1,11,1011,1,110	mAP@50	mAP@50:95	mAP@50	mAP@50:95	1 414 (111)	012015
				0.9754	0.9144	0.9665	0.7196	92.27	147.5
	$\sqrt{}$	√		0.9755 0.9753 0.9766	0.9106 0.9122 0.9087	0.9657 0.9645 0.9715	0.724 0.7205 0.7244	104 113.66 92.27	152 168 147.5
	$\checkmark$	$\sqrt{}$		0.9774 0.9775	0.9022 0.9037	0.9724 0.9728	0.7325 0.7318	104 113.66	152 168
$\sqrt{}$	$\sqrt{}$	$\sqrt{}$	$\checkmark$	0.9778 <b>0.9896</b>	0.903 <b>0.9156</b>	0.9731 <b>0.9851</b>	0.7329 <b>0.7423</b>	125.39 125.39	170 170

### 5.6 Effect of module in the backbone

To clarify why the proposed model does not adopt the more advanced backbone architecture from YOLOv11, which introduces the flexible C3k2 module [51] for feature extraction and integrates a C2PSA attention mechanism [51] at the final stage to consolidate backbone features, ablation studies were conducted across different backbone configurations under identical experimental settings. As demonstrated in Table 5, the baseline C3 architecture achieves optimal performance on both datasets, outperforming variants incorporating YOLOv11's enhanced components. The experimental results demonstrate that optimal results can be achieved by using the C3 module directly.

— Dataset	Backbone	F	Bbox	Mask		
Dataset	Dackbolle	mAP@50	mAP@50:95	mAP@50	mAP@50:95	
DWTAL-s	YOLOv5-backbone YOLOv11-backbone	<b>0.9896</b> 0.978	<b>0.9156</b> 0.9046	<b>0.9851</b> 0.9733	<b>0.7423</b> 0.7295	
DWTAL-l	YOLOv5-backbone YOLOv11-backbone	<b>0.8685</b> 0.8607	<b>0.8017</b> 0.7889	<b>0.8457</b> 0.8379	<b>0.6238</b> 0.6139	

Table 5: Effect of different backbone

### 6 Conclusion

To obtain fine-grained spatial coordinates of cells in deformed tables, we introduce the DWTAL dataset. Addressing the challenges of dense object distributions and extreme scale variations within this dataset, the OG-HFYOLO model is proposed for accurate instance segmentation of tabular cells. The model incorporates several key innovations: the Gradient Orientation-aware Extractor (GOE) enhances contour perception for densely packed objects, the Heterogeneous Kernel Cross-Fusion (HKCF) and scale-aware Loss mitigate the challenges brought by severe scale variation, and a Mask-based Non-Maximum Suppression (MASK-NMS) is employed to prevent erroneous suppression caused by overlapping bounding boxes.

This work leverages instance segmentation to acquire precise spatial coordinates of cells in deformed tables, which is a mid-to-upstream task in table structure recognition. Downstream tasks involving logical coordinate processing can adopt the operational framework of LGPMA, optimizing the workflow through systematic integration of Computer Graphics principles and geometric topology theory. Furthermore, the challenges encountered in the derived dataset, such as dense object arrangements and scale diversity, are prevalent in domains like medical cell segmentation and remote sensing image analysis. Consequently, the proposed framework offers constructive insights for addressing analogous challenges across these fields.

### References

- [1] Mahmoud M. Kasem, Abdelrahman Abdallah, Alexander Berendeyev, Ebrahem Elkady, Mahmoud Abdalla, Mohamed Mahmoud, Mohamed Hamada, Daniyar B. Nurseitov, and Islam Taj-Eddin. Deep learning for table detection and structure recognition: A survey. *ArXiv*, abs/2211.08469, 2022.
- [2] Xu Zhong, Elaheh ShafieiBavani, and Antonio Jimeno Yepes. Image-based table recognition: Data, model, and evaluation. In Andrea Vedaldi, Horst Bischof, Thomas Brox, and Jan-Michael Frahm, editors, *Computer Vision ECCV 2020*, pages 564–580, Cham, 2020. Springer International Publishing.
- [3] Chixiang Ma, Lei Sun, Zhuoyao Zhong, and Qiang Huo. Relatext: Exploiting visual relationships for arbitrary-shaped scene text detection with graph convolutional networks. *Pattern Recognition*, 111:107684, 2021.
- [4] Devashish Prasad, Ayan Gadpal, Kshitij Kapadni, Manish Visave, and Kavita Sultanpure. CascadeTabNet: An approach for end to end table detection and structure recognition from image-based documents. 2020 IEEE/CVF Conference on Computer Vision and Pattern Recognition Workshops (CVPRW), pages 2439–2447, June 2020.
- [5] Liang Qiao, Zaisheng Li, Zhanzhan Cheng, Peng Zhang, Shiliang Pu, Yi Niu, Wenqi Ren, Wenming Tan, and Fei Wu. LGPMA: Complicated table structure recognition with local and global pyramid mask alignment. In Josep Lladós, Daniel Lopresti, and Seiichi Uchida, editors, *Document Analysis and Recognition ICDAR 2021*, volume 12821, pages 99–114, Cham, 2021. Springer International Publishing.

- [6] Rujiao Long, Wen Wang, Nan Xue, Feiyu Gao, Zhibo Yang, Yongpan Wang, and Gui-Song Xia. Parsing table structures in the wild. In 2021 IEEE/CVF International Conference on Computer Vision (ICCV), pages 924–932, Montreal, QC, Canada, October 2021. IEEE.
- [7] TAL Education Group. Tal-ocr-table dataset. https://ai.100tal.com/, 2021.
- [8] Kaiming He, Georgia Gkioxari, Piotr Dollár, and Ross Girshick. Mask r-cnn. *IEEE Transactions on Pattern Analysis and Machine Intelligence*, 42(2):386–397, 2020.
- [9] Daquan Zhou, Qibin Hou, Yunpeng Chen, Jiashi Feng, and Shuicheng Yan. Rethinking bottleneck structure for efficient mobile network design. In Andrea Vedaldi, Horst Bischof, Thomas Brox, and Jan-Michael Frahm, editors, *Computer Vision ECCV 2020*, pages 680–697, Cham, 2020. Springer International Publishing.
- [10] Yuming Chen, Xinbin Yuan, Ruiqi Wu, Jiabao Wang, Qibin Hou, and Mingg-Ming Cheng. Yolo-ms: Rethinking multi-scale representation learning for real-time object detection. *IEEE transactions on pattern analysis and machine intelligence*, PP, 2023.
- [11] Asif Shahab, Faisal Shafait, Thomas Kieninger, and Andreas Dengel. An open approach towards the benchmarking of table structure recognition systems. *ACM*, pages 113–120, 2010.
- [12] Dimosthenis Karatzas, Faisal Shafait, Seiichi Uchida, Masakazu Iwamura, Lluis Gomez i Bigorda, Sergi Robles Mestre, Joan Mas, David Fernandez Mota, Jon Almazàn Almazàn, and Lluís Pere de las Heras. Icdar 2013 robust reading competition. In 2013 12th International Conference on Document Analysis and Recognition, pages 1484–1493, 2013.
- [13] Minghao Li, Lei Cui, Shaohan Huang, Furu Wei, M. Zhou, and Zhoujun Li. Tablebank: Table benchmark for image-based table detection and recognition. *ArXiv*, abs/1903.01949, 2019.
- [14] Yiren Li, Zheng Huang, Junchi Yan, Yi Zhou, Fan Ye, and Xianhui Liu. Gfte: Graph-based financial table extraction. *ArXiv*, abs/2003.07560, 2020.
- [15] Zewen Chi, Heyan Huang, Heng-Da Xu, Houjin Yu, Wanxuan Yin, and Xian-Ling Mao. Complicated table structure recognition. *ArXiv*, abs/1908.04729, 2019.
- [16] Zheng Huang, Kai Chen, Jianhua He, Xiang Bai, Dimosthenis Karatzas, Shijian Lu, and C. V. Jawahar. Icdar2019 competition on scanned receipt ocr and information extraction. *2019 International Conference on Document Analysis and Recognition (ICDAR)*, pages 1516–1520, 2019.
- [17] Wonkyo Seo, Hyung Il Koo, and Nam Ik Cho. Junction-based table detection in camera-captured document images. *International Journal on Document Analysis and Recognition (IJDAR)*, 18:47–57, 2015.
- [18] Yang Wang, Zhikui Ouyang, Runhua Han, Zhijian Yin, and Zhen Yang. Yolomask: Real-time instance segmentation with integrating yolov5 and orienmask. In 2022 IEEE 22nd International Conference on Communication Technology (ICCT), pages 1646–1650, 2022.
- [19] WUJIAN YANG, SUNYANG CHEN, GUANLIN CHEN, and QIHAO SHI. Pr-yolo: Improved yolo for fast protozoa classification and segmentation. *Research Square*, 2023.
- [20] G. Jocher et al. YOLO by ultralytics (version 5.7.0). https://github.com/ultralytics/yolov5, 2022.
- [21] Xianghong Cao, Yixuan Su, Xin Geng, and Yongdong Wang. Yolo-sf: Yolo for fire segmentation detection. *IEEE Access*, 11:111079–111092, 2023.
- [22] Chien-Yao Wang, Alexey Bochkovskiy, and Hong-Yuan Mark Liao. Yolov7: Trainable bag-of-freebies sets new state-of-the-art for real-time object detectors. In 2023 IEEE/CVF Conference on Computer Vision and Pattern Recognition (CVPR), pages 7464–7475, 2023.
- [23] Haoliang Liu, Wei Xiong, and Yu Zhang. Yolo-core: Contour regression for efficient instance segmentation. *Machine Intelligence Research*, 20(5):716–728, 2023.
- [24] Bizhe Bai, Jie Tian, Sicong Luo, Tao Wang, and Sisuo Lyu. Yuseg: Yolo and unet is all you need for cell instance segmentation. In Jun Ma, Ronald Xie, Anubha Gupta, José Guilherme de Almeida, Gary D. Bader, and Bo Wang, editors, *Proceedings of The Cell Segmentation Challenge in Multi-modality High-Resolution Microscopy Images, Competitions in Neural Information Processing Systems*, volume 212 of *Proceedings of Machine Learning Research*, pages 1–15. PMLR, 2022.
- [25] Alexey Bochkovskiy, Chien-Yao Wang, and Hong-Yuan Mark Liao. Yolov4: Optimal speed and accuracy of object detection. *ArXiv*, abs/2004.10934, 2020.
- [26] Wenjun Xia, Peiqing Li, Qipeng Li, Taiping Yang, and Shunfeng Zhang. TTIS-YOLO: a traffic target instance segmentation paradigm for complex road scenarios. *Measurement Science and Technology*, 35(10):105402, October 2024.

- [27] Chengang Dong, Yuhao Tang, and Liyan Zhang. Gha-inst: a real-time instance segmentation model utilizing yolo detection framework. *Cluster Computing*, 27(6):7401–7415, March 2024.
- [28] ITU-R. Studio encoding parameters of digital television for standard 4:3 and wide-screen 16:9 aspect ratios. Recommendation BT.601-7, International Telecommunication Union, 03 2011. Revises BT.601-6 (2007).
- [29] Chien-Yao Wang, Hong-Yuan Mark Liao, Yueh-Hua Wu, Ping-Yang Chen, Jun-Wei Hsieh, and I-Hau Yeh. Cspnet: A new backbone that can enhance learning capability of cnn. In 2020 IEEE/CVF Conference on Computer Vision and Pattern Recognition Workshops (CVPRW), pages 1571–1580, 2020.
- [30] Tsung-Yi Lin, Piotr Dollár, Ross Girshick, Kaiming He, Bharath Hariharan, and Serge Belongie. Feature pyramid networks for object detection. In 2017 IEEE Conference on Computer Vision and Pattern Recognition (CVPR), pages 936–944, 2017.
- [31] Shaoqing Ren, Kaiming He, Ross B. Girshick, and Jian Sun. Faster r-cnn: Towards real-time object detection with region proposal networks. *IEEE Transactions on Pattern Analysis and Machine Intelligence*, 39:1137–1149, 2015.
- [32] Ross Girshick, Jeff Donahue, Trevor Darrell, and Jitendra Malik. Rich feature hierarchies for accurate object detection and semantic segmentation. In 2014 IEEE Conference on Computer Vision and Pattern Recognition, pages 580–587, 2014.
- [33] N. Dalal and B. Triggs. Histograms of oriented gradients for human detection. In 2005 IEEE Computer Society Conference on Computer Vision and Pattern Recognition (CVPR'05), volume 1, pages 886–893, San Diego, CA, USA, 2005. IEEE.
- [34] John S. Bridle. Probabilistic interpretation of feedforward classification network outputs, with relationships to statistical pattern recognition. In Françoise Fogelman Soulié and Jeanny Hérault, editors, *Neurocomputing*, pages 227–236, Berlin, Heidelberg, 1990. Springer Berlin Heidelberg.
- [35] Dmitry Ulyanov, Andrea Vedaldi, and Victor S. Lempitsky. Instance normalization: The missing ingredient for fast stylization. ArXiv, abs/1607.08022, 2016.
- [36] Matthew D. Zeiler and Rob Fergus. Visualizing and understanding convolutional networks. In David Fleet, Tomas Pajdla, Bernt Schiele, and Tinne Tuytelaars, editors, *Computer Vision ECCV 2014*, pages 818–833, Cham, 2014. Springer International Publishing.
- [37] Yuqing Liu, Qi Jia, Xin Fan, Shanshe Wang, Siwei Ma, and Wen Gao. Cross-SRN: Structure-preserving super-resolution network with cross convolution. *IEEE Transactions on Circuits and Systems for Video Technology*, 32(8):4927–4939, August 2022.
- [38] Jiacheng Ruan, Suncheng Xiang, Mingye Xie, Ting Liu, and Yuzhuo Fu. Malunet: A multi-attention and light-weight unet for skin lesion segmentation. 2022 IEEE International Conference on Bioinformatics and Biomedicine (BIBM), pages 1150–1156, 2022.
- [39] Zhaohui Zheng, Ping Wang, Dongwei Ren, Wei Liu, Rongguang Ye, Qinghua Hu, and Wangmeng Zuo. Enhancing geometric factors in model learning and inference for object detection and instance segmentation. *IEEE Transactions on Cybernetics*, 52(8):8574–8586, 2022.
- [40] Yi-Fan Zhang, Weiqiang Ren, Zhang Zhang, Zhen Jia, Liang Wang, and Tieniu Tan. Focal and efficient iou loss for accurate bounding box regression. *Neurocomputing*, 506:146–157, 2022.
- [41] Fausto Milletarì, Nassir Navab, and Seyed-Ahmad Ahmadi. V-net: Fully convolutional neural networks for volumetric medical image segmentation. 2016 Fourth International Conference on 3D Vision (3DV), pages 565–571, 2016.
- [42] Navaneeth Bodla, Bharat Singh, Rama Chellappa, and Larry S. Davis. Soft-nms improving object detection with one line of code. 2017 IEEE International Conference on Computer Vision (ICCV), pages 5562–5570, 2017.
- [43] Xinlong Wang, Rufeng Zhang, Tao Kong, Lei Li, and Chunhua Shen. Solov2: Dynamic, faster and stronger. ArXiv, abs/2003.10152, 2020.
- [44] Kai Chen, Jiaqi Wang, Jiangmiao Pang, Yuhang Cao, Yu Xiong, Xiaoxiao Li, Shuyang Sun, Wansen Feng, Ziwei Liu, Jiarui Xu, Zheng Zhang, Dazhi Cheng, Chenchen Zhu, Tianheng Cheng, Qijie Zhao, Buyu Li, Xin Lu, Rui Zhu, Yue Wu, Kangcheng Liu, Jifeng Dai, Jingdong Wang, Jianping Shi, Wanli Ouyang, Chen Change Loy, and Dahua Lin. Mmdetection: Open mmlab detection toolbox and benchmark. *ArXiv*, abs/1906.07155, 2019.
- [45] Microsoft Research Asia. Torchscale: A toolkit for foundation model training. https://github.com/microsoft/fb.resnet.torch?tab=readme-ov-file#resnet-training-in-torch, 2023. Accessed: 2025-04-18.
- [46] Jia Deng, Wei Dong, Richard Socher, Li-Jia Li, Kai Li, and Li Fei-Fei. Imagenet: A large-scale hierarchical image database. In 2009 IEEE Conference on Computer Vision and Pattern Recognition, pages 248–255, 2009.

- [47] Zhaowei Cai and Nuno Vasconcelos. Cascade r-cnn: High quality object detection and instance segmentation. *IEEE Transactions on Pattern Analysis and Machine Intelligence*, 43(5):1483–1498, 2021.
- [48] Daniel Bolya, Chong Zhou, Fanyi Xiao, and Yong Jae Lee. Yolact: Real-time instance segmentation. In 2019 IEEE/CVF International Conference on Computer Vision (ICCV), pages 9156–9165, 2019.
- [49] Bowen Cheng, Ishan Misra, Alexander G. Schwing, Alexander Kirillov, and Rohit Girdhar. Masked-attention mask transformer for universal image segmentation. In 2022 IEEE/CVF Conference on Computer Vision and Pattern Recognition (CVPR), pages 1280–1289, 2022.
- [50] Rejin Varghese and Sambath M. Yolov8: A novel object detection algorithm with enhanced performance and robustness. In 2024 International Conference on Advances in Data Engineering and Intelligent Computing Systems (ADICS), pages 1–6, 2024.
- [51] Rahima Khanam and Muhammad Hussain. Yolov11: An overview of the key architectural enhancements. *ArXiv*, abs/2410.17725, 2024.
- [52] Lichao Huang, Yi Yang, Yafeng Deng, and Yinan Yu. Densebox: Unifying landmark localization with end to end object detection. *ArXiv*, abs/1509.04874, 2015.